

**Climatology, seasonality, and trends of oceanic coherent
eddies**

Josué Martínez-Moreno¹, Andrew McC. Hogg¹, and Matthew H. England²

⁴ Research School of Earth Science and ARC Center of Excellence for Climate Extremes, Australian
⁵ National University, Canberra, Australia

⁶ Climate Change Research Centre (CCRC), UNSW Australia, Sydney NSW, Australia

7 Key Points:

- ⁸ Kinetic energy of coherent eddies contain around 50% of the surface ocean kinetic
⁹ energy budget.
- ¹⁰ Seasonal cycle of the number of coherent eddies and coherent eddy amplitude re-
¹¹ veal a 3-6 month lag to wind forcing
- ¹² Inverse cascade sets up the seasonal lag of the number and amplitude of coher-
¹³ ent eddies.

14 **Abstract**

15 Ocean eddies influence regional and global climate through mixing and transport
 16 of heat and properties. One of the most recognizable and ubiquitous feature of oceanic
 17 eddies are vortices with spatial scales of tens to hundreds of kilometers, frequently re-
 18 ferred as “mesoscale eddies” or “coherent eddies”. Coherent eddies are known to trans-
 19 port properties across the ocean and to locally affect near-surface wind, cloud proper-
 20 ties and rainfall patterns. Although coherent eddies are ubiquitous, yet their climatol-
 21 ogy, seasonality and long-term temporal evolution remains poorly understood. Thus, we
 22 examine the kinetic energy contained by coherent eddies and we present the annual and
 23 long-term changes of automatically identified coherent eddies from satellite observations
 24 from 1993 to 2019. Around 50% of the kinetic energy contained by ocean eddies corre-
 25 sponds to coherent eddies. Additionally, a strong hemispherical seasonal cycle is observed,
 26 with a 3–6 months lag between the wind forcing and the response of the coherent eddy
 27 field. Furthermore, the seasonality of the number of coherent eddies and their amplitude
 28 reveals that the number of coherent eddies responds faster to the forcing (~ 3 months),
 29 than the coherent eddy amplitude (which is lagged by ~ 6 months). Our analysis high-
 30 lights the relative importance of the coherent eddy field in the ocean kinetic energy bud-
 31 get, implies a strong response of the eddy number and eddy amplitude to forcing at dif-
 32 ferent time-scales, and showcases the seasonality, and multidecadal trends of coherent
 33 eddy properties.

34 **Plain language summary**

35 Coherent eddies are the most common feature in the oceans observable from satel-
 36 lites. They are crucial in ocean dynamics as they can transport properties over long dis-
 37 tances and interact with the atmosphere. Our study investigates the seasonal and long-
 38 term changes in the abundance and intensity of coherent eddies, by automatically iden-
 39 tifying individual eddies over the satellite altimeter record. The seasonal cycle suggests
 40 a transition from numerous, smaller, and weaker coherent eddies, to fewer and larger,
 41 and stronger coherent eddies over the season. In addition, a long-term adjustment of the
 42 coherent eddy field is identified possible due to long-term changes in the climate system.

43 1 Introduction

44 Mesoscale ocean variability with spatial scales of tens to hundreds of kilometers is
 45 comprised of processes such as vortices, waves, and jets (Ferrari & Wunsch, 2009; Fu et
 46 al., 2010). These mesoscale processes are highly energetic, and they play a crucial role
 47 in the transport of heat, salt, momentum, and other tracers through the ocean (Wun-
 48 sch & Ferrari, 2004; Wyrtki et al., 1976; Gill et al., 1974). Possibly, the most recogniz-
 49 able and abundant process observed from satellites is mesoscale vortices. Although mesoscale
 50 vortices are commonly referred to in literature as “mesoscale eddies”, this term is also
 51 often used to describe the total mesoscale ocean variability (the time-varying component
 52 of the mesoscale flow), thus, here we will refer to mesoscale vortices as *coherent eddies*.

53 Coherent eddies are quasi-circular currents. According to their rotational direction,
 54 the sea surface height anomaly within a coherent eddy can have a negative or positive
 55 sea surface height anomaly (cold-core and warm-core coherent eddies, respectively). This
 56 characteristic sea surface height signature of coherent eddies has been utilized to auto-
 57 matically identify and track coherent eddies from satellite altimetry (Cui et al., 2020;
 58 Martínez-Moreno et al., 2019; Ashkezari et al., 2016; Faghmous et al., 2015; Chelton et
 59 al., 2007). Automated identification algorithms of coherent eddies have shown their ubiq-
 60 uity in the oceans, with a predominant influence at hotspots of eddy activity such as bound-
 61 ary extensions and the Antarctic Circumpolar Current. In these regions, Chelton et al.
 62 (2011) estimated that coherent eddies contribute around 40–50% of the mesoscale kinetic
 63 energy (Chelton et al., 2011) and thus a significant fraction of the total kinetic energy
 64 (Ferrari & Wunsch, 2009). Although this unique estimate showcases the importance of
 65 the mesoscale coherent eddy field, the energy contained by coherent eddies was estimated
 66 by extracting the geostrophic velocities within the detected coherent eddies, thus it is
 67 possible it may contain energy from other processes. Coherent eddies are not only abun-
 68 dant and may have a large proportion of the surface kinetic energy budget, but they are
 69 also essential to ocean dynamics as concluded by many previous studies (Patel et al., 2020;
 70 Schubert et al., 2019; Pilo et al., 2015; Frenger et al., 2015, 2013; Beron-Vera et al., 2013;
 71 Siegel et al., 2011; Hogg & Blundell, 2006).

72 There is broad consensus that mesoscale eddy kinetic energy has a pronounced sea-
 73 sonal variability (Uchida et al., 2017; Kang & Curchitser, 2017; Qiu & Chen, 2004; Qiu,
 74 1999). Several hypotheses have been proposed to explain this seasonality including: sea-

75 seasonal variations of atmospheric forcing (Sasaki et al., 2014), seasonality of the mixed layer
76 depth (Qiu et al., 2014; Callies et al., 2015), seasonality of the intensity of barotropic in-
77 stability (Qiu & Chen, 2004), the variability of the baroclinic instability due to the sea-
78 sonality of the vertical shear (Qiu, 1999), and a seasonal lag of the inverse energy cas-
79 cade (i.e. energy is transported between scales, from small to large; Arbic et al., 2013)
80 in combination with the presence of a front in the mixed layer, which can lead to a sea-
81 sonal cycle of the baroclinic instability (Qiu et al., 2014). On one hand, processes such
82 as barotropic and baroclinic instabilities control the seasonality of coherent eddies in the
83 ocean. On the other hand, recent studies using observations and eddy-permitting climate
84 models suggest several long-term adjustments of the global ocean capable of long-term
85 changes in the coherent eddy field. Such readjustments include a multidecadal increase
86 in the ocean stratification resulted from temperature and salinity changes (Li et al., 2020),
87 a horizontal readjustment of the sea surface temperature gradients (Ruela et al., 2020;
88 Bouali et al., 2017; Cane et al., 1997), and an intensification of the kinetic energy, eddy
89 kinetic energy, and mesoscale eddy kinetic energy over the last 3 decades as a consequence
90 of an increase in wind forcing (Hu et al., 2020; Wunsch, 2020; Martínez-Moreno et al.,
91 2021). All these seasonal factors and long-term readjustments directly influence the an-
92 nual and decadal response of the coherent eddy field, however, the seasonality of the co-
93 herent component of the eddy kinetic energy, as well as the seasonal cycle and trends
94 of the coherent eddy statistics remain unknown.

95 Here we present a new global climatology of the coherent eddy kinetic energy by
96 reconstructing the coherent eddy signature from satellite observations. Our study doc-
97 uments the seasonal cycle of the coherent eddy kinetic energy, and seasonal cycle and
98 long-term trends of the coherent eddy properties over the satellite record. Moreover, we
99 conduct more detail analysis in regions where coherent eddies dominate the eddy kinetic
100 energy field. This paper is structured as follows: the data sources and methodology are
101 described in section 2. Then, we present the climatology, energy ratios, and global sea-
102 sonality of the coherent eddy kinetic energy in section 3. Section 4 presents the global
103 climatology and seasonality of coherent eddy properties, followed by long-term changes
104 of the coherent eddy properties (section 5). Then we focus our attention on the seasonal
105 cycle and coherent eddy properties in regions dominated by coherent eddies (section 6).
106 Finally, section 7 summarizes the main results and discusses the implications of this study.

107 **2 Methods**

108 We use daily sea surface height (SSH) data made available by the Copernicus Ma-
 109 rine Environment Monitoring Service in near real time (CMEMS, 2017). This gridded
 110 product contains the sea surface height and geostrophic velocities with daily 0.25° res-
 111 olution from January 1993 to 2019. The daily geostrophic velocities allowed us to com-
 112 pute the kinetic energy (KE) and eddy kinetic energy (EKE) over the satellite record.
 113 The main source of EKE is the time-varying wind (Ferrari & Wunsch, 2009), thus we
 114 computed the seasonal cycle of the wind magnitude from the JRA55 reanalysis (Japan
 115 Meteorological Agency, Japan, 2013) using wind velocities at 10m above the ocean's sur-
 116 face.

117 Over the same record, coherent eddy statistics from Martínez-Moreno et al. (2019),
 118 hereafter M-M, are analyzed and compared to those released by Chelton & Schlax (2013),
 119 both datasets are gridded in a 1° resolution. Although both datasets are produced via
 120 automated eddy identification algorithms using closed contours of SSH, these datasets
 121 have important differences in the criteria they use to identify and record coherent ed-
 122 dies statistics. The major differences include; (i) M-M's algorithm requires an adjust-
 123 ment between a 2D Gaussian and the SSH anomaly (SSHa) surface within the identify
 124 closed contour, while Chelton's only uses the outer-most closed contour of SSH; (ii) M-
 125 M's dataset reports the maximum SSHa within the identified coherent eddy, while Chel-
 126 ton's algorithm reports the maximum SSH value minus the discrete level in which the
 127 coherent eddy was identified; M-M's dataset includes all detected coherent eddies, while
 128 Chelton's dataset excludes (iii) coherent eddies with lifetimes shorter than four weeks
 129 and (iv) coherent eddy amplitudes smaller than 1cm. Moreover, M-M's algorithm allows
 130 the reconstruction of the coherent eddy field under the assumption that coherent eddies
 131 have a 2D Gaussian imprint in the sea surface height. This Gaussian reconstruction of
 132 the coherent eddy field then allow us to estimate the coherent geostrophic eddy veloc-
 133 ities and thus the kinetic energy contained only by coherent eddies.

134 **2.1 Kinetic Energy decomposition**

135 Kinetic energy is commonly divided into the mean and time-varying components
 136 through a Reynolds decomposition. At a given time, the surface velocity field $\mathbf{u} = (u, v)$
 137 is split into the time mean ($\bar{\mathbf{u}}$) and time varying components (\mathbf{u}'). Moreover, M-M pro-

138 posed to further decompose the eddy kinetic energy into the energy contained by coher-
 139 ent features (\mathbf{u}'_e) and non-coherent features (\mathbf{u}'_n). Therefore the KE equation can be writ-
 140 ten as:

$$\text{KE} = \underbrace{\bar{u}^2 + \bar{v}^2}_{\text{MKE}} + \underbrace{u'^2_e + v'^2_e}_{\text{CEKE}} + \underbrace{u'^2_n + v'^2_n}_{\text{nCEKE}} + \mathcal{O}_c^2 + \mathcal{O}^2 \quad (1)$$

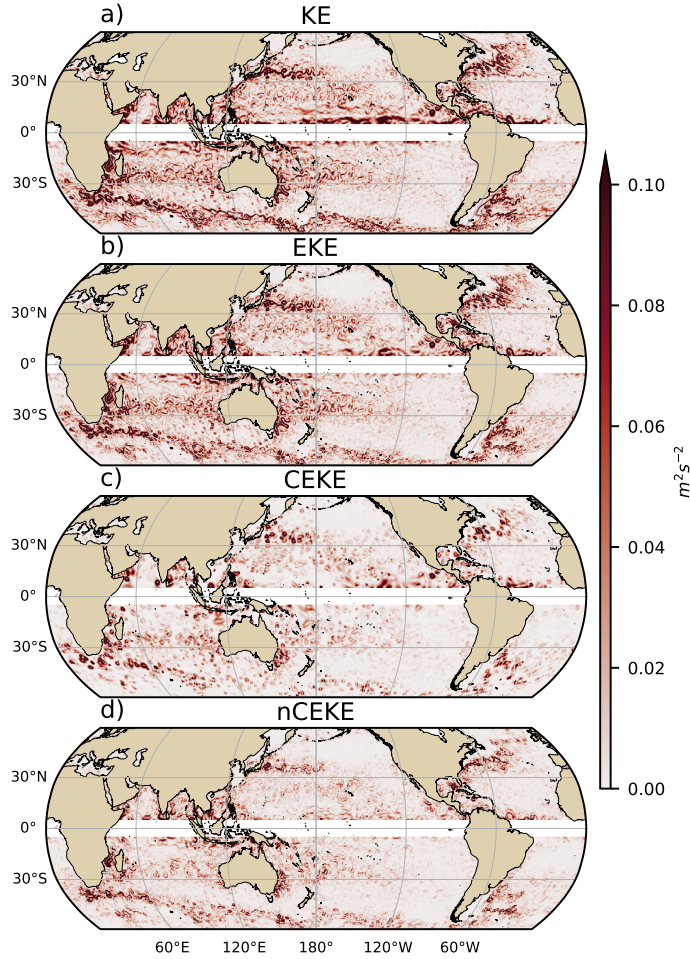
141 Due to the properties of this decomposition, the second order term \mathcal{O}^2 is zero when
 142 averaged over the same period as $\bar{\mathbf{u}}$. However, \mathcal{O}_c^2 is not necessarily negligible, unless it
 143 is averaged over time and space. More information about the decomposition of the field
 144 into coherent features and non-coherent features is explained by Martínez-Moreno et al.
 145 (2019). A global snapshot of each component of kinetic energy decomposition is shown
 146 in Figure 1, where the KE and EKE are comprised of rings and filaments. As expected,
 147 the decomposition of EKE into CEKE and nCEKE components exhibit only ring-like
 148 signatures expected of coherent eddies, while the non-coherent component shows filaments
 149 and some miss-identified coherent eddies.

153 2.2 Eddy statistics

154 The eddy statistics used in this study include (i) the eddy count ($cEddy_n$) defined
 155 as the number of eddies per grid cell, (ii) the eddy diameter defined as the diameter of
 156 a circle with equal area as the closed contour of each identified eddy, and (iii) the mean
 157 eddy amplitude defined as the mean amplitude of the coherent eddies within the cell ($cEddy_{amp}$).
 158 The latter metric can be separated into positive ($cEddy_{amp}^+$) and negative ($cEddy_{amp}^-$)
 159 coherent eddy amplitudes, defined as the mean amplitude of warm core and cold core
 160 coherent eddies, respectively, within the cell. The polarity independent eddy amplitude
 161 ($|cEddy_{amp}|$) is defined as:

$$|cEddy_{amp}| = \frac{1}{2} (cEddy_{amp}^+ - cEddy_{amp}^-) \quad (2)$$

162 Note that the $cEddy_{amp}^+$ and $cEddy_{amp}^-$ are sign definite, thus the difference will always
 163 be positive, the gridded averaged $cEddy_{amp}$ can be negative or positive noting the dom-
 164 inant polarity of coherent eddies in the region, and the absolute $cEddy_{amp}$ is denoted
 165 by $cEddy_{|amp|}$. We analyze the climatology, seasonal cycles and trends of the eddy statis-
 166 tics between 1993 and 2019. We exclude the equatorial region (10°S - 10°N) and pole-



150 **Figure 1.** Snapshot of surface kinetic energy ($\overline{\text{KE}}$), surface eddy kinetic energy ($\overline{\text{EKE}}$),
 151 surface coherent eddy kinetic energy ($\overline{\text{CEKE}}$), and surface non-coherent eddy kinetic energy
 152 ($\overline{\text{nCEKE}}$) for the 1st of January 2017.

167 ward of 60° . Note that the climatology of cEddy_n is computed by adding all the iden-
 168 tified eddies over the record, while all other climatological statistics are computed as the
 169 time-average over the record. Seasonal climatologies are calculated for the monthly av-
 170 erage of each coherent eddy statistic, while hemispherical time-series are filtered with
 171 a running average of 90 days. Trends of cEddy_n and $|\text{cEddy}_{amp}|$ are calculated by coars-
 172 ening the dataset to a 5° grid, and then linear trends are computed for each grid point,
 173 the statistical significance is assessed by a modified Mann-Kendall test (Yue & Wang,
 174 2004).

175 Time averages are denoted by $\overline{}$, while area-weighted averages are denoted using
 176 $\langle \rangle$, the area weighted of function f is:

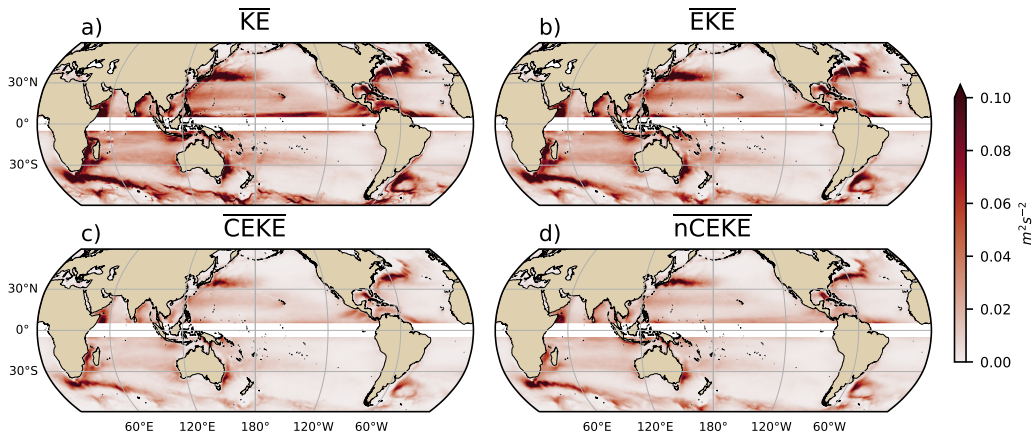
$$\langle f \rangle = \frac{\int f dx dy}{\int dx dy}, \quad (3)$$

177 area-weighted coherent eddy properties masked areas each time, where no coherent ed-
 178 dies were identified.

179 3 Global Coherent Eddy Energetics

180 The kinetic energy decomposition estimated from sea surface height measured by
 181 satellite altimeters is shown in Figure 2. These maps show that many regions of the global
 182 ocean are highly energetic in mean KE (\overline{KE}), mean EKE (\overline{EKE}), mean coherent eddy
 183 kinetic energy (\overline{CEKE}) and mean non-coherent eddy kinetic energy (\overline{nCEKE}). The spa-
 184 tial pattern highlights well known regions of the ocean where mesoscale processes are abun-
 185 dant, such as the western boundary extensions and the Antarctic Circumpolar Current.
 186 Remarkably, the spatial distribution of the energy contained by the reconstructed mesoscale
 187 coherent eddies and non-coherent components are similar (Figures 2c,d). However, there
 188 are some regions where coherent eddies dominate over non-coherent, and vice-versa. Over-
 189 all, this decomposition suggest that boundary current extensions and other energetic re-
 190 gions, in particularly, eddy-rich regions in the ocean contain both coherent and non-coherent
 191 components of the kinetic energy.

204 Eddy kinetic energy is known to be more than an order of magnitude greater than
 205 MKE (Gill et al., 1974); this result is clearly shown in Figure 3a, where \overline{EKE} is respon-
 206 sible for almost all the \overline{KE} across the ocean, except for regions with persistent currents
 207 over time. Such regions are located in the mean boundary extension locations, the equa-
 208 torial Pacific currents and regions in the Antarctic Circumpolar Current, where the \overline{EKE}
 209 explains around 40% of the \overline{KE} . In a previous study, Chelton et al. (2011) estimated that
 210 the EKE within coherent eddies with lifetimes greater than 4 weeks contain between 40
 211 to 60 percent of the \overline{EKE} . Our method to reconstruct the coherent eddy signature (Fig-
 212 ure 3b) further corroborates that the coherent component ($\langle \overline{CEKE} \rangle$) has $\sim 48\%$ of the
 213 $\langle \overline{KE} \rangle$ (Figure 3d). Furthermore, global area averages of the ratios show $\langle \overline{EKE} \rangle$ explains
 214 $\sim 78\%$ of the ocean $\langle \overline{KE} \rangle$ field, while non coherent eddy features contain $\sim 57\%$ percent
 215 of the $\langle \overline{EKE} \rangle$. Note the globally averaged coherent and non coherent components do not
 216 add to 100% as the cross terms (\mathcal{O}_c^2) are non-zero, due to coherent eddy reconstruction

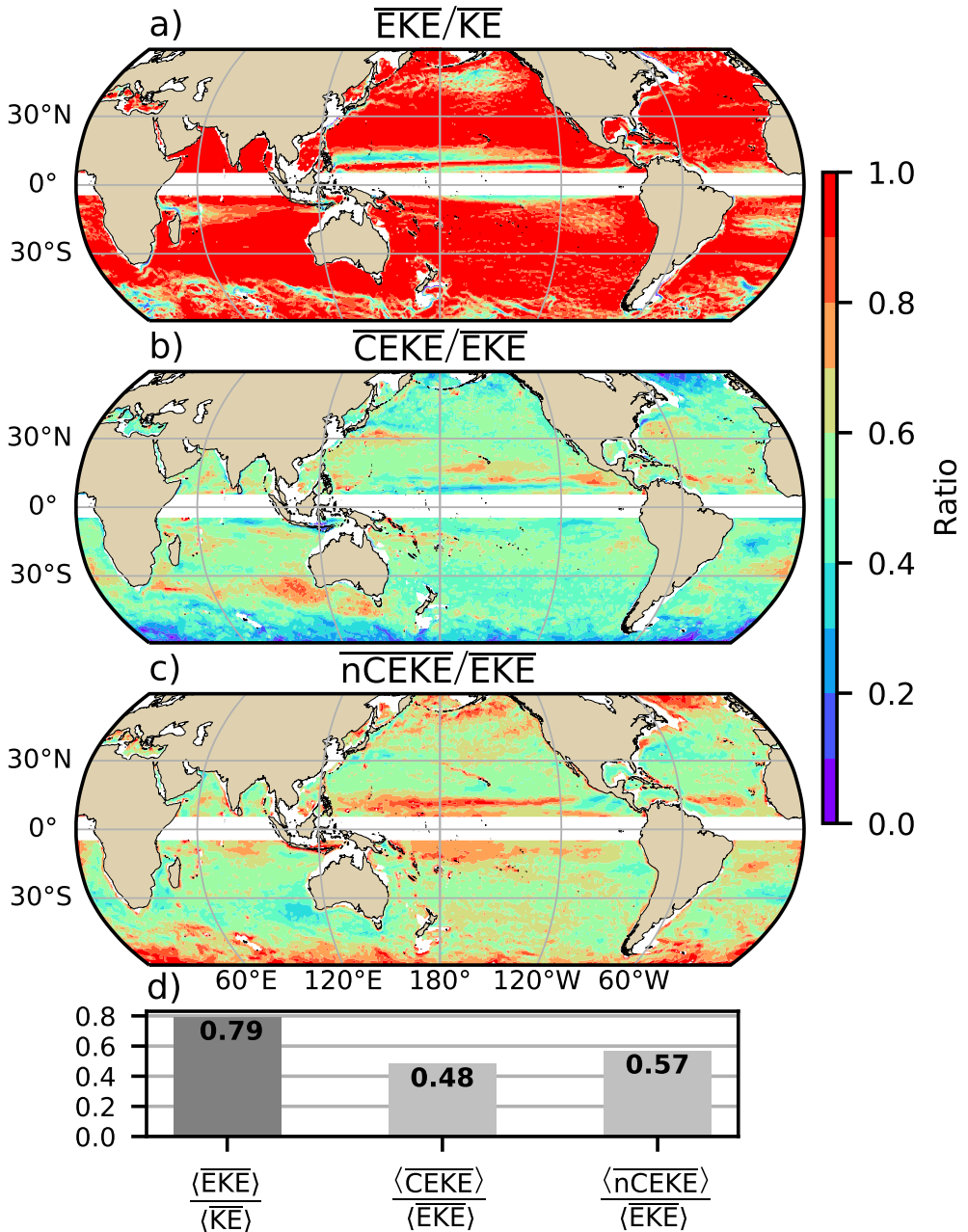


192 **Figure 2.** Mean surface kinetic energy (\overline{KE}), surface eddy kinetic energy (\overline{EKE}), surface
193 coherent eddy kinetic energy (\overline{CEKE}), and surface non-coherent eddy kinetic energy (\overline{nCEKE})
194 between 1993-2018.

217 errors. The spatial pattern reveals a dominance of the \overline{CEKE} equatorward from the bound-
218 ary extensions and areas with large coherent eddy contributions of around 80% of the
219 region's eddy kinetic energy can be found south of Australia, the Tehuantepec Gulf, and
220 the tropical Atlantic. An evident signal is an reduction of the energy contained by co-
221 herent eddies at high latitudes and an increase in the energy explained by non-coherent
222 eddies; this signal could be a consequence of the incapability of the 0.25° satellite res-
223 olution (~ 13 km at 60°) to resolve coherent eddies with scales smaller than ~ 10 km (first
224 baroclinic Rossby radius at 60° ; Chelton et al. 1998).

225 Figure 4 shows the seasonal cycle of the area weighted EKE and CEKE for the North-
226 ern Hemisphere ($\langle EKE \rangle_{NH}$ and $\langle CEKE \rangle_{NH}$; $10^\circ N - 60^\circ N$) and Southern Hemisphere
227 ($\langle EKE \rangle_{SH}$ and $\langle CEKE \rangle_{SH}$; $60^\circ S - 10^\circ S$). In both hemispheres, the $\langle EKE \rangle$ and $\langle CEKE \rangle$
228 peak during summer. In the Northern Hemisphere, the largest $\langle EKE \rangle_{NH}$ and $\langle CEKE \rangle_{NH}$
229 occurs in July, ~ 6 months after the maximum winds in January (purple bar and back
230 star in Figure 4c and d). Meanwhile, the Southern Ocean $\langle EKE \rangle_{SH}$ and $\langle CEKE \rangle_{SH}$ sea-
231 sonal maxima arises during December, ~ 4 months after the maximum winds in August
232 (purple bar and back star in Figure 4g, and h). This lag between winds and the eddy
233 and coherent eddy energy components is further discussed in section 4.

234 The cyclic plots in Figure 4 show the temporal evolution of $\langle EKE \rangle$ and $\langle CEKE \rangle$.
235 Note that high frequency variability can be observed in the $\langle CEKE \rangle$ field with tempo-



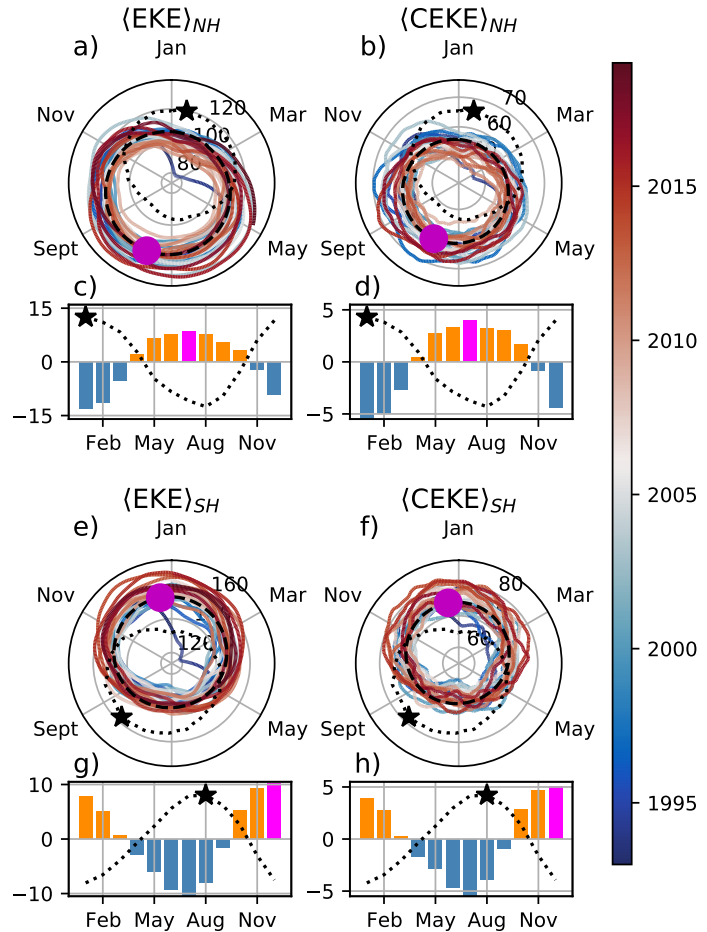
195 **Figure 3.** Ratios of the kinetic energy components. a) Map of the proportion of mean eddy
 196 kinetic energy ($\overline{\text{EKE}}$) versus mean kinetic energy ($\overline{\text{KE}}$); b) Map of the percentage of mean co-
 197 herent eddy kinetic energy ($\overline{\text{CEKE}}$) versus mean eddy kinetic energy ($\overline{\text{EKE}}$); c) Map of the
 198 percentage of mean non-coherent eddy kinetic energy ($\overline{\text{nCEKE}}$) versus mean eddy kinetic energy
 199 ($\overline{\text{EKE}}$); d) Global time and area averaged (represented by $\langle \rangle$) percentage of mean eddy kinetic
 200 energy ($\langle \overline{\text{EKE}} \rangle$) versus the global mean kinetic energy ($\langle \overline{\text{KE}} \rangle$), area averaged percentage of mean
 201 coherent eddy kinetic energy ($\langle \overline{\text{CEKE}} \rangle$) and mean non coherent eddy kinetic energy ($\langle \overline{\text{nCEKE}} \rangle$)
 202 versus global mean eddy kinetic energy ($\langle \overline{\text{EKE}} \rangle$). Regions where the depth of the ocean is shall-
 203 lower than 1000m are removed from the ratio estimation.

236 ral scales of a few months, this could be attributed local dynamics averaged over the hemi-
 237 sphere, as well as errors within the coherent eddy reconstruction. Additionally, concen-
 238 tric changes in the cyclic plots highlight long-term changes over the record. For exam-
 239 ple, the Northern Hemisphere winters in early years of the record (blue) had a more en-
 240 ergetic coherent eddy field, which has transitioned to weaker coherent energy contents
 241 since 2010 (red), in other words, the intensity of the $\langle \text{CEKE} \rangle_{NH}$ field has decreased. A
 242 larger long-term change can be observed in the Southern Hemisphere, where concentric
 243 growth over time in $\langle \text{EKE} \rangle_{SH}$ and $\langle \text{CEKE} \rangle_{SH}$ support the previously observed strength-
 244 ening of the eddy field in the Southern Ocean (Hogg et al., 2015; Martínez-Moreno et
 245 al., 2019; Martínez-Moreno et al., 2021).

255 4 Global Coherent Eddy Statistics

256 Coherent eddy kinetic energy allows us to quantify and study the energy of the eddy
 257 field, but the coherent eddy properties computed by automated coherent eddy identi-
 258 fication algorithms allow us investigate in more detail the contribution and temporal changes
 259 of their abundance (the number of eddies) and their intensity (both their amplitude and
 260 diameter). Figure 5 shows gridded climatologies of the number of eddies and the eddy
 261 amplitude. We contrast our M-M eddy count with Chelton et al. (2007) (Figure 5a-b).
 262 Although the number of the identified eddies is larger in M-M, possibly due to the life-
 263 span filter implemented by Chelton, both datasets reveal consistent spatial patterns. For
 264 example, both datasets show high abundance of eddies in the East North Pacific, East
 265 North Atlantic, as well as the East South Pacific, East South Atlantic and East Indian
 266 Ocean, and small number counts of eddies in the tropics and in high latitudes ($\sim 60^\circ$).
 267 An interesting pattern also emerges in both eddy count datasets, where small scale struc-
 268 tures with larger eddy counts are favored across the ocean. In addition, to preferential
 269 coherent eddy paths observable in boundary extensions and regions in the Southern Ocean.
 270 These clusters and paths of coherent eddies could be associated with topographic fea-
 271 tures, however they remain a puzzling consistency between the eddy count pattern us-
 272 ing these two eddy identification methods.

278 Regions with large counts of eddies have in general small absolute amplitudes (Fig-
 279 ure 5 c), ocean gyre interiors follow with a larger absolute amplitude and finally regions
 280 such as the boundary extensions and Antarctic Circumpolar Current have the largest
 281 coherent eddy absolute amplitudes as shown by Chelton et al. (2011). Eddy amplitude



246 **Figure 4.** Seasonality of the area weighted eddy kinetic energy ($\langle EKE \rangle$), coherent eddy ki-
 247 netic energy ($\langle CEKE \rangle$). Panels a and b show the time-series of the Northern Hemisphere, while
 248 panels e and f correspond to the Southern Hemisphere. Panels c and d show the seasonal cycle of
 249 the $\langle EKE \rangle_{NH}$ and $\langle CEKE \rangle_{NH}$ in the Northern Hemisphere, and panels g and h show the South-
 250 ern Hemisphere ($\langle EKE \rangle_{SH}$ and $\langle CEKE \rangle_{SH}$). Dashed lines correspond to the seasonal cycle of the
 251 fields and dotted lines show the seasonal cycle of the wind magnitude smoothed over 120 days
 252 (moving average). The black and magenta markers (circle and bar) show the maximum of the
 253 seasonal cycle for the kinetic energy components and the wind magnitude, respectively. In cyclic
 254 plots, line colors shows the year.

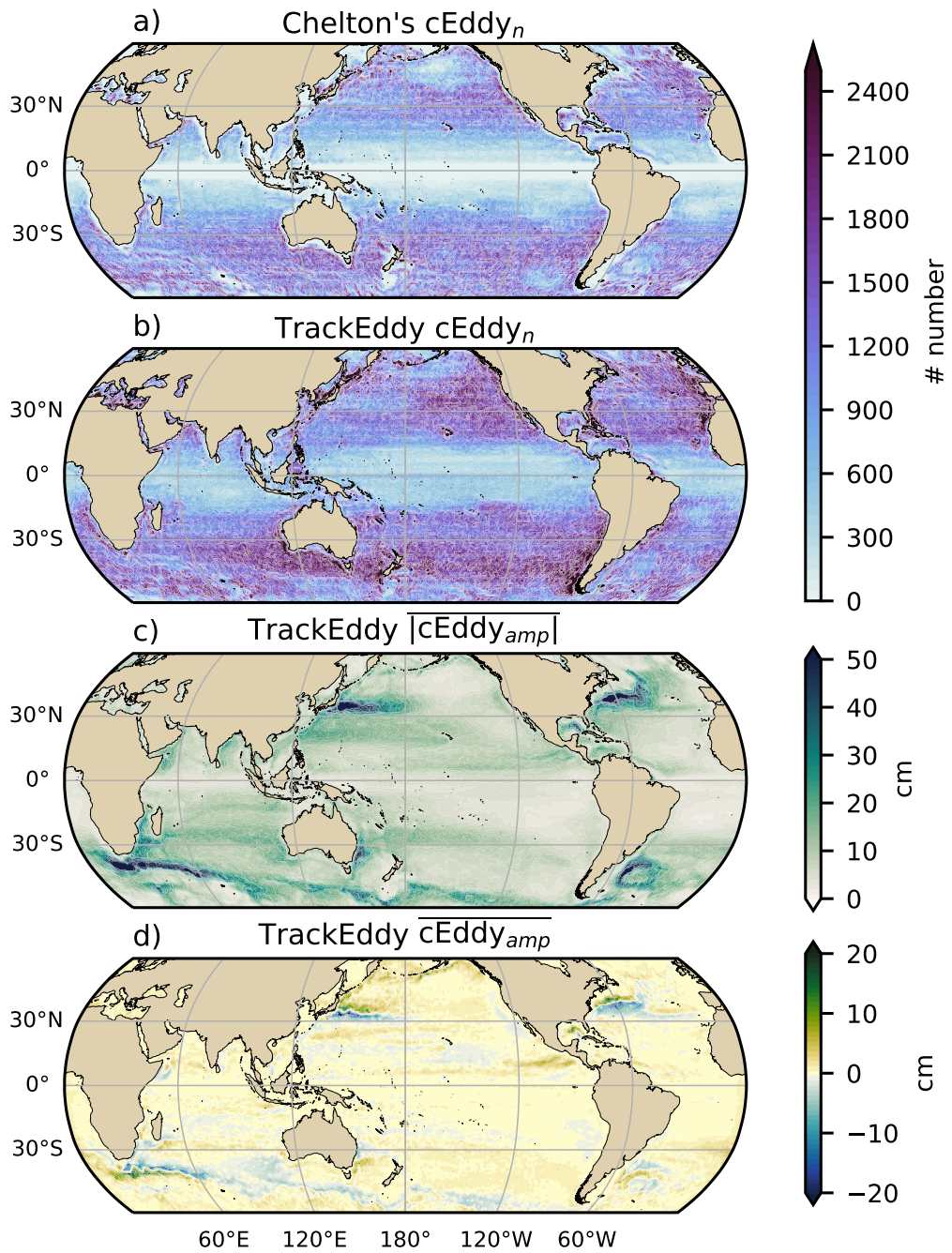


Figure 5. Averaged coherent eddy statistics. a) Climatology of the number of coherent eddies ($cEddy_n$) identified by Chelton et al. (2007); b) Climatology of the number of coherent eddies ($cEddy_n$) identified by Martínez-Moreno et al. (2019); c) Climatology of the mean absolute coherent eddy amplitude ($cEddy_{amp}$). d) Climatology of the mean coherent eddy amplitude ($cEddy_{amp}$).

highlights regions dominated by a given coherent eddy polarity, for example, boundary extensions have a preferred sign (Figure 5 d); positive amplitude polewards of the boundary extension mean location, and negative amplitude equatorwards. This sign preference is consistent with the preferential way coherent eddies are shed from boundary extensions; warm core eddies (positive) polewards of the boundary current extension, and equatorward for cold core eddies (negative) (Kang & Curchitser, 2013; Chelton et al., 2011, 2007). These global statistics reveal the absolute coherent eddy amplitude is a proxy of the CEKE with similar spatial patterns (Figure 2 & Figure 5 c) and showcases that regions where $\overline{\text{CEKE}}$ has a large proportion of $\overline{\text{EKE}}$ (Figure 3), the absolute coherent eddy amplitude is also large.

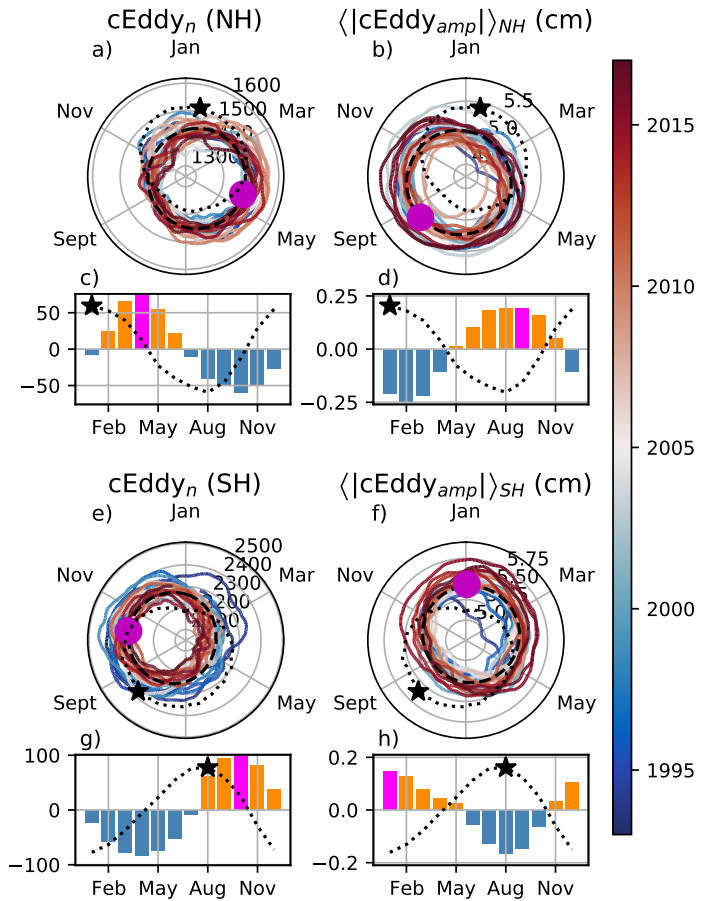
To further understand the seasonal cycle of $\langle \text{CEKE} \rangle$, we compute the climatology of coherent eddy properties in each hemisphere (Figure 6). The seasonality of the number of eddies in the Northern Hemisphere peaks on April (Figure 6 a, c), while the Southern Hemisphere maximum number of eddies occurs during October (Figure 6 e, g). Meanwhile, the seasonality of the polarity independent eddy amplitude ($\langle |c\text{Eddy}_{amp}| \rangle$) peaks in August and January for the Northern and Southern Hemispheres respectively (Figure 6 b, d, f, and h). As expected, the seasonality of $\langle |c\text{Eddy}_{amp}| \rangle_{xw}$, or equivalent to the intensity of the coherent eddies, is consistent with the seasonal cycle of $\langle \text{CEKE} \rangle$. Furthermore, a distinct lag of ~ 3 months is observed between the winds and eddy count, while the eddy amplitude maximum occurs ~ 6 months after the seasonal maxima in winds. We observe the eddy number increases earlier in the year and through eddy-eddy interactions (merging of coherent eddies) the amplitude of the coherent eddy increases ~ 3 months after. This seasonal lag and summer maxima is consistent with Figure 5, furthermore, previous studies suggest that a time-lag of the inverse cascade (Sasaki et al., 2014; Qiu et al., 2014) is responsible of the EKE seasonal cycle, where winter has the highest energy at the smallest scales (non-resolvable with satellite observations), spring and autumn have the highest and lowest energy in scales of 50-100 km, and summertime has the highest energy at the largest scales (> 100 km; Uchida et al. 2017). Thus, the maximum of $\langle \text{EKE} \rangle$, $\langle \text{CEKE} \rangle$, and $\langle |c\text{Eddy}_{amp}| \rangle$ located during summertime suggest that the seasonality of eddies and coherent eddies could be dominated by scales larger than 100 km. This result can be further explored by looking at the seasonal evolution of the eddy diameter ($c\text{Eddy}_d$). Note that 90% of identified coherent eddies have diameters between 50 to 220 km (Figure 7 a). We divided eddies into large-scale coherent eddies (di-

315 ameter > 120 km) and small-scale coherent eddies (diameter < 120 km; Figure 7a). In
 316 the Northern Hemisphere, small eddies have a seasonal peak in diameter during May,
 317 while large eddies have the greatest diameter in September (Figure 7 b). Meanwhile, in
 318 the Southern Hemisphere, the small-scale coherent eddies have the maximum diameter
 319 in December, while large-scale coherent eddies peak in February (Figure 7 c). This re-
 320 sult suggests that wind driven baroclinic instabilities generate small coherent eddies early
 321 in the season, which then merge and grow to become larger in diameter and amplitude,
 322 and thus, more energetic. This process is associated with the inverse energy cascade, and
 323 suggest that this mechanism not only drives the EKE seasonality, but also may be re-
 324 sponsible of the seasonal cycle of coherent eddies.

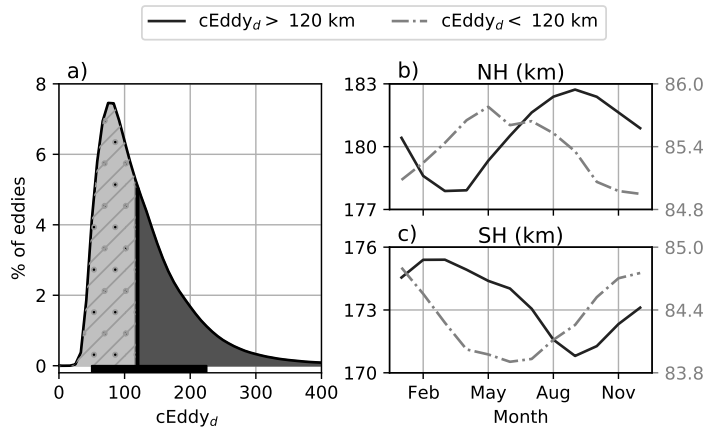
325 Long-term changes can be observed in Figure 6a,b, e, and f where growing-shrinking
 326 concentric circles over time denote an increase-decrease trend of the field. This trend is
 327 particularly evident in the Southern Hemisphere, where the number of eddies has decreased,
 328 the eddy amplitude has increased. This result is consistent with the observed trends in
 329 EKE and mesoscale EKE in the Southern Ocean (Hogg et al., 2015; Martínez-Moreno
 330 et al., 2019).

331 Seasonality of the area weighted eddy kinetic energy ($\langle \text{EKE} \rangle$), coherent eddy ki-
 332 netic energy ($\langle \text{CEKE} \rangle$). Panels a and b show the time-series of the Northern Hemisphere,
 333 while panels e and f correspond to the Southern Hemisphere. Panels c and d show the
 334 seasonal cycle of the $\langle \text{EKE} \rangle_{NH}$ and $\langle \text{CEKE} \rangle_{NH}$ in the Northern Hemisphere, and pan-
 335 els g and h show the Southern Hemisphere ($\langle \text{EKE} \rangle_{SH}$ and $\langle \text{CEKE} \rangle_{SH}$). Dashed lines
 336 correspond to the seasonal cycle of the fields and dotted lines show the seasonal cycle
 337 of the wind magnitude smoothed over 120 days (moving average). The black and ma-
 338 genta markers (circle and bar) show the maximum of the seasonal cycle for the kinetic
 339 energy components and the wind magnitude, respectively. In cyclic plots, line colors shows
 340 the year.

356 The coherent eddy amplitude from positive coherent eddies and negative coherent
 357 eddies show similar seasonal cycles to the absolute eddy amplitude. The Northern Hemis-
 358 phere decrease in absolute eddy amplitude is driven by a decrease of the amplitude of
 359 negative coherent eddies in the Northern Hemisphere. Meanwhile in the Southern Ocean,
 360 the increase in absolute eddy amplitude is corroborated by an strengthening of both co-
 361 herent eddy polarities since the early 90s.



341 **Figure 6.** Seasonality of the count of number of eddies ($cEddy_n$) and area weighted polarity
 342 independent coherent eddy amplitude ($\langle |cEddy_{amp}| \rangle$); Panels a and b show the time-series of the
 343 Northern Hemisphere, while panels e and f correspond to the Southern Hemisphere. Panels c
 344 and d show the seasonal cycle of the $cEddy_n$ and $\langle |cEddy|_{amp} \rangle_{NH}$ in the Northern Hemisphere,
 345 and panels g and h show the Southern Hemisphere ($cEddy_n$ and $\langle |cEddy|_{amp} \rangle_{SH}$). Dashed lines
 346 correspond to the seasonal cycle of the fields and dotted lines show the seasonal cycle of the
 347 wind magnitude smoothed over 120 days (moving average). The black and magenta markers
 348 (circle and bar) show the maximum of the seasonal cycle for the eddy property and the wind
 349 magnitude, respectively. In cyclic plots, line colors shows the year.



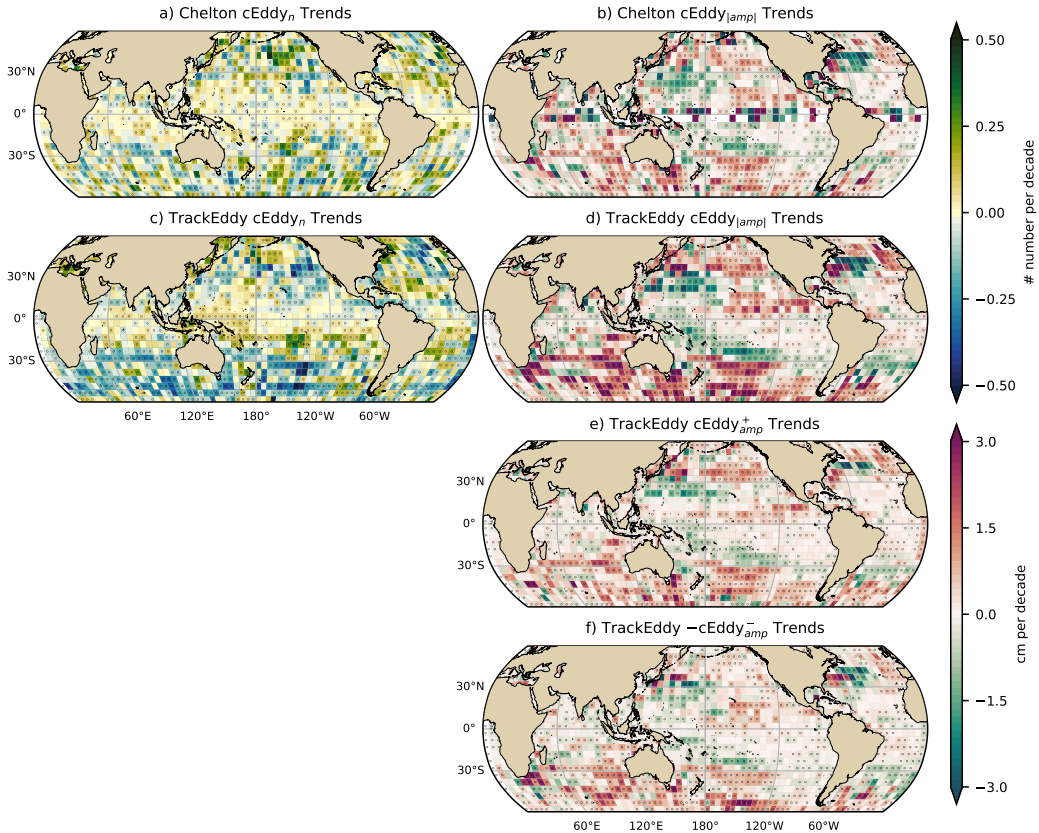
350 **Figure 7.** Distribution of the identified eddy diameter ($cEddy_d$; km) and hemispherical
 351 seasonality of the coherent eddy diameter. a) Distribution in percentage of identified eddy am-
 352 plitude, solid bar below distribution represents 90% of the identified eddies. Seasonal cycle of
 353 the eddy diameter for the b) Northern Hemisphere and c) Southern Hemisphere. Dark solid line
 354 and area corresponds to coherent eddies with diameters larger than 120 km, while light gray
 355 dash-dotted line and area shows coherent eddies with diameters smaller than 120 km.

362 5 Trends

363 The results presented in Figures 4 and 6 suggest a long-term readjustment of the
 364 coherent eddy field. The long-term trends of the number of coherent eddies, absolute co-
 365 herent eddy amplitude, and coherent eddy amplitude polarities are explored in Figure
 366 8. Chelton's and M-M datasets show consistent spatial patterns in the trends and sig-
 367 nificance of the number of coherent eddies and the absolute coherent eddy amplitude.
 368 Several regions in the ocean, such as the Southern Ocean, North Atlantic and North Pa-
 369 cific, show a decrease in the number of eddies. Those same regions also have a clear in-
 370 crease in the absolute coherent eddy amplitude. These trends are similar to those ob-
 371 served in mesoscale eddy kinetic energy (Martínez-Moreno et al., 2021) and provide ad-
 372 dditional evidence of a readjustment of the mesoscale eddy field over the last 3 decades.

373 *@Matt: What do you think? Is it important to highlight the trends we observe are
 374 different to sea level rise? Or is the next paragraph irrelevant?*

375 The observed trends of $cEddy_{amp}$ in several oceanic regions have the same scale
 376 as sea level rise (~3cm per decade) by analyzing the positive and negative coherent eddy



385 **Figure 8.** Trends of coherent eddy statistics. a) and b) Trends of the number of identified
 386 coherent eddies from satellite observations identified using TrackEddy, and those reported in
 387 Chelton’s dataset. c) and d) Trends of the absolute value of identified coherent eddies amplitude
 388 ($cEddy_{amp}$) from satellite observations identified using TrackEddy, and those reported
 389 in Chelton’s dataset. e) and f) Trends of eddy amplitude polarity using TrackEddy ($cEddy_{amp}^+$
 390 and $cEddy_{amp}^-$). Gray stippling shows regions that are statistically significant above the 95%
 391 confidence level.

377 amplitude we can discard the observed trends correspond to an increase in sea level. In
 378 fact, each coherent eddy polarity has intensified in the Southern Ocean and North East
 379 Pacific and Atlantic. In other words, the amplitude of each polarity has increased over
 380 time, thus this strengthening is an intrinsic response of the coherent eddy field. Note that
 381 the negative coherent eddy amplitude dominates the global $|cEddy_{amp}|$ trends (Figure
 382 8e, f). However, different trend pattern can be observed in both positive and negative
 383 coherent eddy amplitudes in the north Atlantic and north Pacific, where the negative
 384 coherent eddy amplitude in the Western Boundary Currents appears to decrease.

392 **6 Regional Climatology**

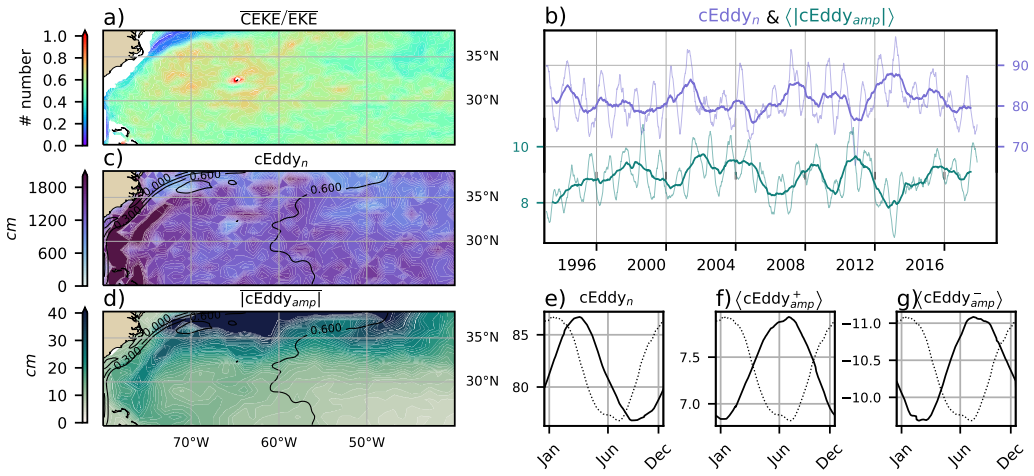
393 For regions with relatively large proportions of CEKE located at boundary exten-
 394 sions and eastern currents, we investigate the seasonal and long-term variability of the
 395 coherent eddy properties.

396 The most energetic western boundary extensions include; the Gulf Stream, the Kuroshio
 397 Current, and the Agulhas Current (Figures 9, 10, and 11). Coherent eddy generation in
 398 boundary extensions occurs through baroclinic and barotropic instabilities of the mean
 399 current, thus all these regions share similar generation dynamics. In all these regions with-
 400 out exception; (i) CEKE contains up to 80% of the EKE in regions equatorwards from
 401 the mean western boundary extension location, (ii) the number of eddies is consistently
 402 minimal numbers of eddies over the mean western boundary extension location, and (iii)
 403 the eddy amplitude is larger polewards of the mean western boundary extension loca-
 404 tion.

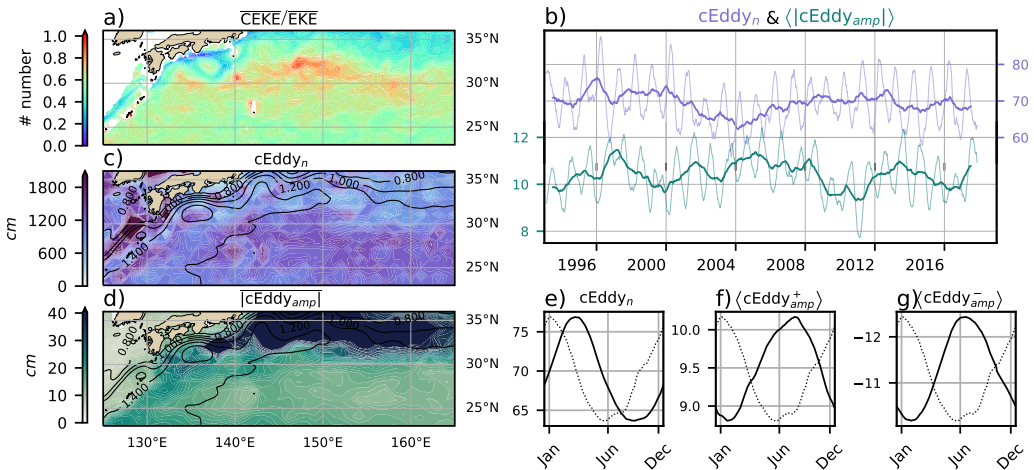
405 In the Gulf Stream, the energy ratio between CEKE and EKE is \sim 56% (Figure 9).
 406 The highest energy content occurs in regions with numerous eddies, and collocated with
 407 regions where the largest $|cEddy_{amp}|$ gradients occurs. The time series of $cEddy_n$ and
 408 $\langle |cEddy_{amp}| \rangle$ are anti-correlated (-0.52), and they display inter-annual and seasonal vari-
 409 ability. Although Chaudhuri et al. (2009) observed a positive phase of North Atlantic
 410 Oscillation (NAO) exhibit higher EKE, due to an increase in baroclinic instabilities, thus
 411 suggesting more coherent eddies, we do not find a correlation between the $cEddy_n$ or the
 412 $\langle |cEddy_{amp}| \rangle$ in the Gulf Stream and the NAO index. Similar to the signal observed in
 413 the hemispherical analysis, the eddy count seasonal cycle follows the wind maximum af-
 414 ter \sim 3 months, while the amplitude of the coherent eddies lags by \sim 6 months.

423 The variability of the $cEddy_n$ and $\langle |cEddy_{amp}| \rangle$ in the Kuroshio Current are weakly
 424 anti-correlated (-0.41; Figure 10). However, on average 56% of the energy in the region
 425 corresponds to CEKE. As observed in the Gulf Stream, there is an important seasonal
 426 cycle in the boundary extensions, where the eddy count seasonal cycle occurs on March
 427 after \sim 3 months of the wind maximum (January). Meanwhile, the amplitude of the co-
 428 herent eddies lags by \sim 6 months (June) after the maximum wind.

435 In the Southern Hemisphere, the strongest boundary current, the Agulhas Current
 436 shows similar behavior to its counterparts in the Northern Hemisphere (Figure 11). On



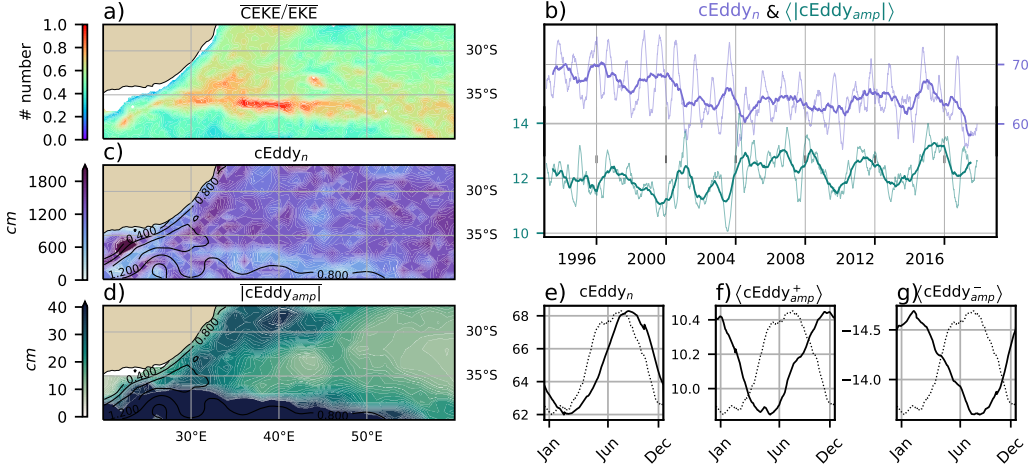
415 **Figure 9.** Climatology of the eddy field and coherent eddy field at the Gulf Stream. a) Ra-
 416 tio of mean coherent eddy kinetic energy ($\overline{\text{CEKE}}$) versus mean eddy kinetic energy ($\overline{\text{EKE}}$); b)
 417 Thick lines show the running average over 2 years and thin lines show the running average over
 418 90 days of the coherent eddy number sum and the average coherent eddy amplitude; c) Map of
 419 the number of eddies; d) Map of the average coherent eddy amplitude; e) Seasonal cycle of the
 420 number of eddies f) Seasonal cycle of the positive coherent eddy amplitude. g) Seasonal cycle of
 421 the negative coherent eddy amplitude. Contours in maps correspond to mean sea surface height
 422 (m).



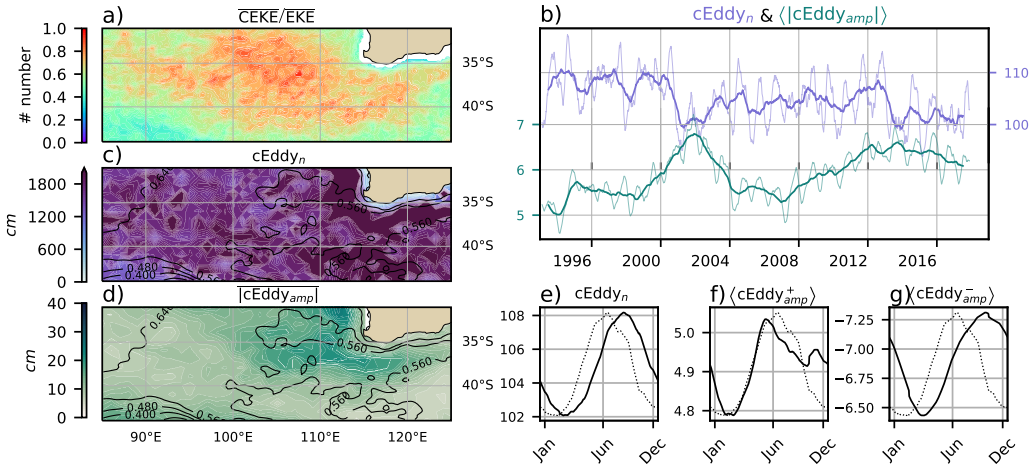
429 **Figure 10.** Climatology of the eddy field and coherent eddy field at the Kuroshio extension.
430 a) Ratio of mean coherent eddy kinetic energy ($\overline{\text{CEKE}}$) versus mean eddy kinetic energy ($\overline{\text{EKE}}$);
431 b) Time-series of the coherent eddy number and the average coherent eddy amplitude; c) Map of
432 the number of eddies; d) Map of the average coherent eddy amplitude; Seasonal cycle of the e)
433 number of eddies, f) positive coherent eddy amplitude, and g) negative coherent eddy amplitude.
434 Different lines represent the same as in Figure 9.

437 average, coherent eddies in the Agulhas current contain $\sim 56\%$ of the energy, meanwhile
438 the cEddy_n seasonal peak occurs in August, while the $\langle |c\text{Eddy}_{amp}| \rangle$ occurs in January-
439 February. The seasonal lag between the winds, eddy count, and eddy amplitude in each
440 of the western boundary current extensions is interpreted as being analogous to the ex-
441 planation observed in Figure 6 of the lagged response of coherent eddy properties due
442 to eddy-eddy interactions, consistent with the inverse cascade of energy.

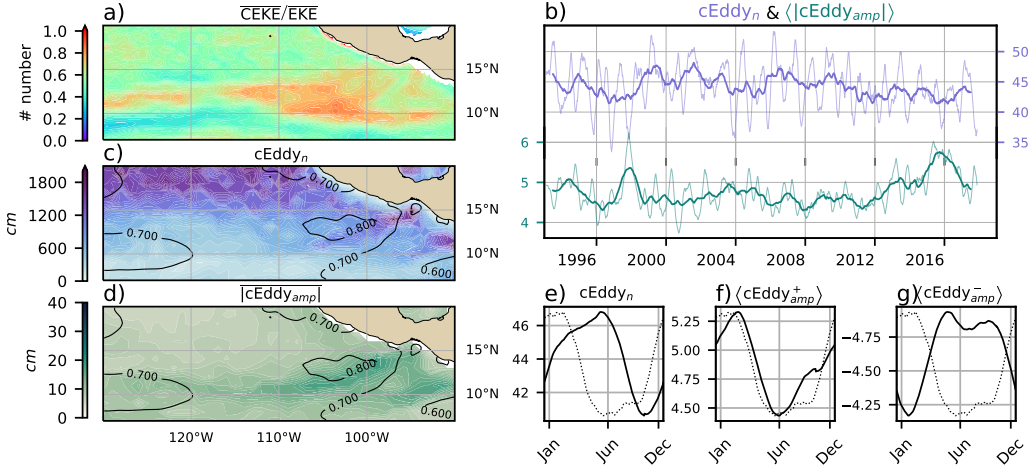
449 Coherent eddies dominate the EKE field in other regions such as the Leeuwin Cur-
450 rent (Figure 12), where the 65% of the energy is contained by coherent eddies. Although
451 the Leeuwin region is not characterized by having a large EKE, however, a considerable
452 abundance of eddies and large eddy amplitudes are observable in the region. The series
453 reveal a significant increase in the $\langle |c\text{Eddy}_{amp}| \rangle$, while the cEddy_n has decreased over
454 the last 3 decades (@Andy, you suggested a reference here, I couldn't find it....). The
455 seasonal cycle shows that the cEddy_n peak occurs on August, 3 months after the max-
456 imum winds (June). Meanwhile, the $\langle \text{cEddy}_{amp}^+ \rangle$ responds in synchrony to winds, and
457 the $\langle \text{cEddy}_{amp}^- \rangle$ is in phase with the seasonal cycle of the cEddy_n .



443 **Figure 11.** Climatology of the eddy field and coherent eddy field at the Agulhas Current. a)
444 Ratio of mean coherent eddy kinetic energy ($\overline{\text{CEKE}}$) versus mean eddy kinetic energy ($\overline{\text{EKE}}$); b)
445 Time-series of the coherent eddy number and the average coherent eddy amplitude; c) Map of
446 the number of eddies; d) Map of the average coherent eddy amplitude; Seasonal cycle of the e)
447 number of eddies, f) positive coherent eddy amplitude, and g) negative coherent eddy amplitude.
448 Different lines represent the same as in Figure 9.



458 **Figure 12.** Climatology of the eddy field and coherent eddy field at the Leeuwin Current. a)
459 Ratio of mean coherent eddy kinetic energy ($\overline{\text{CEKE}}$) versus mean eddy kinetic energy ($\overline{\text{EKE}}$); b)
460 Time-series of the coherent eddy number and the average coherent eddy amplitude; c) Map of
461 the number of eddies; d) Map of the average coherent eddy amplitude; Seasonal cycle of the e)
462 number of eddies, f) positive coherent eddy amplitude, and g) negative coherent eddy amplitude.
463 Different lines represent the same as in Figure 9.



477 **Figure 13.** Climatology of the eddy field and coherent eddy field at the East Tropical Pacific.
 478 a) Ratio of mean coherent eddy kinetic energy ($\overline{\text{CEKE}}$) versus mean eddy kinetic energy ($\overline{\text{EKE}}$);
 479 b) Time-series of the coherent eddy number and the average coherent eddy amplitude; c) Map of
 480 the number of eddies; d) Map of the average coherent eddy amplitude; Seasonal cycle of the e)
 481 number of eddies, f) positive coherent eddy amplitude, and g) negative coherent eddy amplitude.
 482 Different lines represent the same as in Figure 9.

464 Another region with important contributions of the coherent eddy field is the East
 465 Tropical Pacific (Tehuantepec region; Figure 13), where coherent eddies contain $\sim 58\%$
 466 of the energy. In fact, coherent eddy generation in this region is modulated by winds and
 467 coastally trapped waves which produce a strong horizontal and vertical shear (baroclinic
 468 and barotropic instabilities; Zamudio et al., 2006). Furthermore, the equatorial gener-
 469 ated waves propagating along the coast have an important interannual variability ob-
 470 servable in the $\langle |c\text{Eddy}_{amp}| \rangle$ time-series, where El Niño events are notable during 1997
 471 and 2015 (Figure 13b). The seasonal cycle of $c\text{Eddy}_n$, $\langle c\text{Eddy}_{amp}^+ \rangle$, and $\langle c\text{Eddy}_{amp}^- \rangle$ sup-
 472 port the idea of a coherent eddies responding to two different coherent eddy generation
 473 mechanisms; the number of eddies seasonal cycle lags for by ~ 3 months from the winds,
 474 while the $\langle c\text{Eddy}_{amp}^+ \rangle$ is on phase with the winds and the maximum of trapped waves
 475 (winter; Zamudio et al., 2006), and the $\langle c\text{Eddy}_{amp}^- \rangle$ could be a consequence of eddy-eddy
 476 interactions.

483 **7 Discussion and Conclusions**

484 We investigated the contribution of coherent eddies in the kinetic energy field us-
 485 ing satellite observations. We corroborate that around half of the EKE is explained by
 486 coherent eddies. This half is concentrated in eddy-rich regions where an intensification
 487 of the eddy field has been observed (Martínez-Moreno et al., 2021). The energy contained
 488 by eddies is larger than the previous estimate of 40% by Chelton et al. (2011). Although
 489 there are difference in the identification criteria of both eddy identification methods, the
 490 main cause of the difference is believed to be the lifespan and amplitude filters. These
 491 filters are widely used to track individual eddies on space and time, however, interactions
 492 between eddies in energetic regions my obscure the abundance and influence of short-
 493 lived coherent eddies. Filters are not used in this study, and indeed a lack of filters could
 494 facilitates an under or over-estimation of the the energy contained by coherent eddies,
 495 when miss-identifying or miss-fitting a coherent eddy. Thus, the presented estimate rep-
 496 resents an upper limit of the energy contained by coherent eddies.

497 In addition, it should be noted that regions with first baroclinic Rossby radius of
 498 deformation smaller than 10km cannot be resolved by satellite observations. Thus, the
 499 energy contained by coherent eddies around latitudes of 60° and those near the shore
 500 are missed from this estimate, and remains unknown their role in the seasonal cycle and
 501 local dynamics. New satellite altimeter missions (SWOT) may allow to estimate energy
 502 contained by mesoscale coherent eddies outside the tropical region and the continental
 503 slope.

504 Hemispherical variability indicates a strong seasonal cycle of the EKE, CEKE, and
 505 eddy properties. The seasonal cycle of the CEKE in each hemisphere occurs as a con-
 506 sequence of numerous small coherent eddies interacting with each other (eddy-eddy in-
 507 teractions) and resulting in stronger, larger and more energetic coherent eddies during
 508 summer after a few months of the yearly coherent eddy number maxima. This results
 509 reveals eddy-eddy interactions and thus the transfer of energy from smaller coherent ed-
 510 dries to larger coherent eddies could explain the observed seasonal cycle of CEKE and
 511 coherent eddies properties.

512 Coherent eddy properties showcase a non-uniform long-term readjustment of the
 513 mesoscale eddy field. Overall, the eddy number has decreased globally at a significant
 514 rate of ~ 35 eddies per decade from ~ 4000 eddies identified globally on average each day.

515 However, large proportions of the ocean show an strengthening of the mesoscale coher-
516 ent eddy field at a rate greater than ~ 1 cm per decade. This strengthening of the co-
517 herent eddy amplitude is attributed to an intensification of each coherent eddy polar-
518 ity, rather than a readjustment of the coherent eddy field to sea level rise. In other words,
519 the coherent eddy amplitude intensification is occurring in both coherent eddy polar-
520 ities and explain a proportion of the previously observed readjustments in the eddy field
521 to long-term changes in the ocean forcing (Hu et al., 2020; Wunsch, 2020; Martínez-Moreno
522 et al., 2021). This long-term readjustment showcases an intensification of the coherent
523 eddy field, possibly due to long-term readjustments in the ocean baroclinic and barotropic
524 instabilities, as well as the strength of the winds.

525 The reconstruction of the coherent eddies and their statistics have revealed regions
526 with important coherent eddy contributions and a distinct seasonal evolution of the co-
527 herent eddies. Remarkably, western boundary extensions generate eddies through the
528 instability of the main currents and the seasonal cycle of coherent eddies, CEKE, and
529 thus EKE could be associated with an inverse energy cascade observable through lagged
530 seasonal cycles in the coherent eddy statistics. In addition to this, the amplitude of the
531 seasonal cycle in the boundary extensions is two times larger than any other region, thus
532 the seasonality of the coherent eddies in boundary extensions dominate the hemispher-
533 ical seasonal cycle. Furthermore, the seasonal lag of the inverse energy cascade is cou-
534 pled with the presence of fronts, such is the case of western boundary extensions, and
535 our results are consistent with the notion of baroclinic instability generating eddies and
536 through eddy-eddy interactions an lagged inverse energy cascade.

537 The use of satellite observations in this study limit our ability to quantify the im-
538 portance of the inverse energy cascade seasonality in the control of the coherent eddy
539 seasonal cycle. As mentioned above, there is robust evidence of an increase in eddy-eddy
540 interactions, however we can not discard important contributions from other processes
541 such as the seasonal cycle of forcing and instabilities, which are crucial in the genera-
542 tion of coherent eddies. Although this study can provide a descriptive response of the
543 coherent eddy field, further studies are needed to asses the role of eddy-eddy interactions
544 in our changing climate, ocean dynamics, and biogeochemical process. Furthermore, the
545 SWOT mission could allow to advance our understanding of eddy-eddy interactions and
546 the seasonal cycle of scales smaller than mesoscale, which may provide further evidence
547 of the inverse energy cascade driving the coherent eddy seasonality.

548 **Acknowledgments**

549 Chelton & Schlax (2013) dataset was produced by SSALTO/DUACS and distributed by
 550 AVISO+ (<https://www.aviso.altimetry.fr/>) with support from CNES, developed
 551 and validated in collaboration with E.Mason at IMEDEA. Global coherent eddy recon-
 552 struction, coherent and non-coherent eddy kinetic energy datasets, in addition to grid-
 553 ded coherent eddy tracking datasets are publicly available at (<https://doi.org/10.5281/zenodo.4646429>). All analyses and figures in this manuscript are reproducible via Jupyter
 554 notebooks and instructions can be found in the Github repository CEKE_climatology
 555 (https://github.com/josuemtzmo/CEKE_climatology). Trends used the Python Pack-
 556 age xarrayMannKendall (<https://doi.org/10.5281/zenodo.4458776>)
 557

558 **References**

- 559 Arbic, B. K., Polzin, K. L., Scott, R. B., Richman, J. G., & Shriver, J. F. (2013).
 560 On Eddy Viscosity, Energy Cascades, and the Horizontal Resolution of Gridded
 561 Satellite Altimeter Products*. *Journal of Physical Oceanography*, 43(2), 283–300.
 562 doi: 10.1175/jpo-d-11-0240.1
- 563 Ashkezari, M. D., Hill, C. N., Follett, C. N., Forget, G., & Follows, M. J. (2016).
 564 Oceanic eddy detection and lifetime forecast using machine learning methods.
 565 *Geophysical Research Letters*, 43(23). doi: 10.1002/2016gl071269
- 566 Beron-Vera, F. J., Wang, Y., Olascoaga, M. J., Goni, G. J., & Haller, G. (2013). Ob-
 567 jective Detection of Oceanic Eddies and the Agulhas Leakage. *Journal of Physical
 568 Oceanography*, 43(7), 1426–1438. doi: 10.1175/JPO-D-12-0171.1
- 569 Bouali, M., Sato, O. T., & Polito, P. S. (2017). Temporal trends in sea surface tem-
 570 perature gradients in the South Atlantic Ocean. *Remote Sensing of Environment*,
 571 194, 100–114. doi: 10.1016/j.rse.2017.03.008
- 572 Callies, J., Flierl, G., Ferrari, R., & Fox-Kemper, B. (2015). The role of mixed-layer
 573 instabilities in submesoscale turbulence. *Journal of Fluid Mechanics*, 788, 5–41.
 574 doi: 10.1017/jfm.2015.700
- 575 Cane, M. A., Clement, A. C., Kaplan, A., Kushnir, Y., Pozdnyakov, D., Seager, R.,
 576 ... Murtugudde, R. (1997). Twentieth-Century Sea Surface Temperature Trends.
 577 *Science*, 275(5302), 957–960. doi: 10.1126/science.275.5302.957
- 578 Chaudhuri, A. H., Gangopadhyay, A., & Bisagni, J. J. (2009). Interannual variabil-
 579 ity of Gulf Stream warm-core rings in response to the North Atlantic Oscillation.

- 580 *Continental Shelf Research*, 29(7), 856–869. doi: 10.1016/j.csr.2009.01.008
- 581 Chelton, D. B., A. d. R., Schlax, M. G., Naggar, K., & Siwetz, N. (1998). Geographical
582 variability of the first baroclinic Rossby radius of deformation. *Journal*
583 of *Physical Oceanography*, 28(3), 433-460. doi: 10.1175/1520-0485(1998)028<433:
584 GVOTFB>2.0.CO;2
- 585 Chelton, D. B., Gaube, P., Schlax, M. G., Early, J. J., & Samelson, R. M. (2011).
586 The influence of nonlinear mesoscale eddies on near-surface oceanic chlorophyll.
587 *Science*, 334(6054), 328-32. doi: 10.1126/science.1208897
- 588 Chelton, D. B., & Schlax, M. G. (2013). *Mesoscale eddies in altimeter observations*
589 of *ssh*.
- 590 Chelton, D. B., Schlax, M. G., Samelson, R. M., & de Szoeke, R. A. (2007). Global
591 observations of large oceanic eddies. *Geophysical Research Letters*, 34(15),
592 L15606. doi: 10.1029/2007GL030812
- 593 CMEMS. (2017). The Ssalto/Duacs altimeter products were produced and dis-
594 tributed by the Copernicus Marine and Environment Monitoring Service. *Aviso*
595 Dataset. Retrieved from <https://www.aviso.altimetry.fr/>
- 596 Cui, W., Wang, W., Zhang, J., & Yang, J. (2020). Identification and census statis-
597 tics of multicore eddies based on sea surface height data in global oceans. *Acta*
598 *Oceanologica Sinica*, 39(1), 41–51. doi: 10.1007/s13131-019-1519-y
- 599 Faghmous, J. H., Frenger, I., Yao, Y., Warmka, R., Lindell, A., & Kumar, V. (2015,
600 6). A daily global mesoscale ocean eddy dataset from satellite altimetry. *Scientific*
601 *Data*, 2, 150028 EP -. doi: 10.1038/sdata.2015.28
- 602 Ferrari, R., & Wunsch, C. (2009). Ocean Circulation Kinetic Energy: Reservoirs,
603 Sources, and Sinks. *Annual Review of Fluid Mechanics*, 41(1), 253–282. doi: 10
604 .1146/annurev.fluid.40.111406.102139
- 605 Frenger, I., Gruber, N., Knutti, R., & Münnich, M. (2013). Imprint of Southern
606 Ocean eddies on winds, clouds and rainfall. *Nature Geoscience*, 6(8), 608 EP -.
607 doi: 10.1038/ngeo1863
- 608 Frenger, I., Münnich, M., Gruber, N., & Knutti, R. (2015). Southern Ocean eddy
609 phenomenology. *Journal of Geophysical Research: Oceans*, 120(11), 7413-7449.
610 doi: 10.1002/2015JC011047
- 611 Fu, L., Chelton, D., Le Traon, P., & Oceanography, M. R. (2010). Eddy dynamics
612 from satellite altimetry. *Oceanography*, 23(4), 14-25. doi: 10.2307/24860859

- 613 Gill, A., Green, J., & Simmons, A. (1974). Energy partition in the large-scale ocean
614 circulation and the production of mid-ocean eddies. *Deep Sea Res Oceanogr Abstr*,
615 21(7), 499-528. doi: 10.1016/0011-7471(74)90010-2
- 616 Hogg, A. M., & Blundell, J. R. (2006). Interdecadal variability of the southern
617 ocean. *Journal of Physical Oceanography*, 36(8), 1626-1645. doi: 10.1175/
618 JPO2934.1
- 619 Hogg, A. M., Meredith, M. P., Chambers, D. P., Abrahamsen, E. P., Hughes,
620 C. W., & Morrison, A. K. (2015). Recent trends in the Southern Ocean
621 eddy field. *Journal of Geophysical Research: Oceans*, 120(1), 257-267. doi:
622 10.1002/2014JC010470
- 623 Hu, S., Sprintall, J., Guan, C., McPhaden, M. J., Wang, F., Hu, D., & Cai,
624 W. (2020, 2). Deep-reaching acceleration of global mean ocean circula-
625 tion over the past two decades. *Science Advances*, 6(6), eaax7727. doi:
626 10.1126/sciadv.aax7727
- 627 Japan Meteorological Agency, Japan. (2013). *Jra-55: Japanese 55-year reanalysis,*
628 *daily 3-hourly and 6-hourly data.* Boulder CO: Research Data Archive at the Na-
629 tional Center for Atmospheric Research, Computational and Information Systems
630 Laboratory. Retrieved from <https://doi.org/10.5065/D6HH6H41>
- 631 Kang, D., & Curchitser, E. N. (2013). Gulf stream eddy characteristics in a high-
632 resolution ocean model. *Journal of Geophysical Research: Oceans*, 118(9), 4474-
633 4487. Retrieved from <https://agupubs.onlinelibrary.wiley.com/doi/abs/10.1002/jgrc.20318> doi: <https://doi.org/10.1002/jgrc.20318>
- 634 Kang, D., & Curchitser, E. N. (2017). On the Evaluation of Seasonal Variability of
635 the Ocean Kinetic Energy. *Geophysical Research Letters*, 47, 1675-1583. doi: 10
636 .1175/JPO-D-17-0063.1
- 637 Li, G., Cheng, L., Zhu, J., Trenberth, K. E., Mann, M. E., & Abraham, J. P. (2020).
638 Increasing ocean stratification over the past half-century. *Nature Climate Change*,
639 1-8. doi: 10.1038/s41558-020-00918-2
- 640 Martínez-Moreno, J., Hogg, A. M., England, M., Constantinou, N. C., Kiss, A. E.,
641 & Morrison, A. K. (2021). Global changes in oceanic mesoscale currents over the
642 satellite altimetry record. *Journal of Advances in Modeling Earth Systems*, 0(ja).
643 doi: 10.1029/2019MS001769
- 644 Martínez-Moreno, J., Hogg, A. M., Kiss, A. E., Constantinou, N. C., & Morrison,
645

- 646 A. K. (2019). Kinetic energy of eddy-like features from sea surface altimetry. *Journal of Advances in Modeling Earth Systems*, 11(10), 3090-3105. doi: 10.1029/2019MS001769
- 647
- 648
- 649 Patel, R. S., Llort, J., Strutton, P. G., Phillips, H. E., Moreau, S., Pardo, P. C., & Lenton, A. (2020). The Biogeochemical Structure of Southern Ocean Mesoscale Eddies. *Journal of Geophysical Research: Oceans*, 125(8). doi: 10.1029/2020jc016115
- 650
- 651
- 652
- 653 Pilo, G. S., Mata, M. M., & Azevedo, J. L. L. (2015). Eddy surface properties and propagation at Southern Hemisphere western boundary current systems. *Ocean Science*, 11(4), 629–641. doi: 10.5194/os-11-629-2015
- 654
- 655
- 656 Qiu, B. (1999). Seasonal Eddy Field Modulation of the North Pacific Subtropical Counter-current: TOPEX/Poseidon Observations and Theory. *Journal of Physical Oceanography*, 29(10), 2471–2486. doi: 10.1175/1520-0485(1999)029<2471:sefmot>2.0.co;2
- 657
- 658
- 659
- 660 Qiu, B., & Chen, S. (2004). Seasonal Modulations in the Eddy Field of the South Pacific Ocean. *Journal of Physical Oceanography*, 34(7), 1515–1527. doi: 10.1175/1520-0485(2004)034<1515:smitef>2.0.co;2
- 661
- 662
- 663 Qiu, B., Chen, S., Klein, P., Sasaki, H., & Sasai, Y. (2014). Seasonal Mesoscale and Submesoscale Eddy Variability along the North Pacific Subtropical Counter-current. *Journal of Physical Oceanography*, 44(12), 3079–3098. doi: 10.1175/JPO-D-14-0071.1
- 664
- 665
- 666
- 667 Ruela, R., Sousa, M. C., deCastro, M., & Dias, J. M. (2020). Global and regional evolution of sea surface temperature under climate change. *Global and Planetary Change*, 190, 103190. doi: 10.1016/j.gloplacha.2020.103190
- 668
- 669
- 670 Sasaki, H., Klein, P., Qiu, B., & Sasai, Y. (2014). Impact of oceanic-scale interactions on the seasonal modulation of ocean dynamics by the atmosphere. *Nature Communications*, 5(1), 5636. doi: 10.1038/ncomms6636
- 671
- 672
- 673 Schubert, R., Schwarzkopf, F. U., Baschek, B., & Biastoch, A. (2019). Submesoscale Impacts on Mesoscale Agulhas Dynamics. *Journal of Advances in Modeling Earth Systems*, 11(8), 2745–2767. doi: 10.1029/2019ms001724
- 674
- 675
- 676 Siegel, D., Peterson, P., DJ, M., Maritorena, S., & Nelson, N. (2011). Bio-optical footprints created by mesoscale eddies in the Sargasso Sea. *Geophysical Research Letters*, 38(13), n/a-n/a. doi: 10.1029/2011GL047660
- 677
- 678

- 679 Uchida, T., Abernathey, R., & Smith, S. (2017). Seasonality of eddy kinetic energy
680 in an eddy permitting global climate model. *Ocean Modelling*, 118, 41–58. doi: 10
681 .1016/j.ocemod.2017.08.006
- 682 Wunsch, C. (2020). Is The Ocean Speeding Up? Ocean Surface Energy Trends.
683 *Journal of Physical Oceanography*, 50(11), 1–45. doi: 10.1175/jpo-d-20-0082.1
- 684 Wunsch, C., & Ferrari, R. (2004). Vertical mixing, energy, and the general circulation
685 of the oceans. *Annual Review of Fluid Mechanics*, 36(1), 281–314. doi: 10
686 .1146/annurev.fluid.36.050802.122121
- 687 Wyrtki, K., Magaard, L., & Hager, J. (1976). Eddy energy in the oceans. *Journal of
688 Geophysical Research*, 81(15), 2641–2646. doi: 10.1029/JC081i015p02641
- 689 Yue, S., & Wang, C. (2004). The Mann-Kendall Test Modified by Effective Sample
690 Size to Detect Trend in Serially Correlated Hydrological Series. *Water Resources
691 Management*, 18(3), 201–218. doi: 10.1023/b:warm.0000043140.61082.60
- 692 Zamudio, L., Hurlbut, H. E., Metzger, E. J., Morey, S. L., O'Brien, J. J., Tilburg,
693 C., & Zavala-Hidalgo, J. (2006). Interannual variability of Tehuantepec ed-
694 dies. *Journal of Geophysical Research: Oceans (1978–2012)*, 111(C5). doi:
695 10.1029/2005JC003182